



Wave-packet dynamics in a non-Hermitian exciton-polariton system

Y.-M. Robin Hu , Elena A. Ostrovskaya, and Eliezer Estrecho *

ARC Centre of Excellence in Future Low-Energy Electronics Technologies and Department of Quantum Science and Technology, Research School of Physics, The Australian National University, Canberra, ACT 2601, Australia



(Received 24 October 2022; revised 20 July 2023; accepted 26 July 2023; published 5 September 2023)

We theoretically investigate the dynamics of wave packets in a generic, non-Hermitian, optically anisotropic exciton-polariton system that exhibits degeneracies of its complex-valued eigenenergies in the form of pairs of exceptional points in momentum space. We observe the self-acceleration and reshaping of the wave packets governed by their eigenenergies. We further find that the exciton-polariton wave packets tend to evolve into the eigenstate with the smaller decay rate, then propagate towards the minima of the decay rates in momentum space, resulting in directional transport in real space. We also describe the formation of pseudospin topological defects on the imaginary Fermi arc, where the decay rates of the two eigenstates coincide in momentum space. These effects of non-Hermiticity on the dynamics of exciton polaritons can be observed experimentally in a microcavity with optically anisotropic cavity spacer or exciton-hosting materials. This rich non-Hermitian dynamics can also be observed in other two-dimensional, two-band systems with similar complex band structures such as purely photonic planar microcavities, liquid crystal cavities, and non-Hermitian photonic lattices.

DOI: [10.1103/PhysRevB.108.115404](https://doi.org/10.1103/PhysRevB.108.115404)

I. INTRODUCTION

Open dissipative systems described by non-Hermitian Hamiltonian operators can feature novel phenomena not possible in conservative, Hermitian systems [1–4], such as novel topological invariants [3–7], new topological states [1,3,4,6–11], nontrivial lasing [2,12,13], and unidirectional transport [2,12,14,15], to name a few. Most of these effects can be traced back to the complex-valued eigenvalues of the non-Hermitian Hamiltonian. The imaginary part of the energy eigenvalues determines the growth or decay rate of the corresponding eigenstate and hence strongly affects the dynamics of the system, even in the absence of an external potential. For example, a recent study on a non-Hermitian Dirac model showed that a wave packet can move in momentum space without the presence of an external force as a result of the growth and decay of its components [16]. The trajectories of the wave packets under this self-acceleration are polarization dependent and the center-of-mass (COM) momenta for certain initial conditions follow the gradient of the imaginary part of the eigenenergy. Similar effects were also described in the context of a one-dimensional non-Hermitian lattice [17]. Nontrivial dynamical effects due to non-Hermiticity are therefore expected to arise in experimental systems with gain and loss.

A suitable experimental platform for investigating non-Hermitian dynamics in a continuous two-dimensional medium is microcavity exciton polaritons (polaritons herein), which are electron-hole pairs (excitons) strongly coupled to photons in an optical microcavity [5,18–20]. Polaritons represent an accessible solid-state platform for studies of non-Hermitian physics due to their inherent open-dissipative character [5,21–26]. The peak energies and linewidths of the

polariton emission spectra correspond to the real and imaginary parts of the energy eigenvalues [5,21], respectively. Direct imaging of real- and momentum-space density and phase distributions is also possible, augmented by the time and polarization resolution. These capabilities have already enabled measurements of non-Hermitian spectral degeneracies, both in parameter and momentum space, as well as the associated topological invariants and pseudospin textures [5,21,27]. Experiments showed that the dispersion of lower polaritons in anisotropic systems forms two momentum-space bands corresponding to the two components of the polariton pseudospin (polarization), which can display spectral degeneracies in the form of pairs of exceptional points [5,27,28] connected by the so-called Fermi arcs [5], i.e., the lines of degeneracy in the imaginary parts of the eigenenergies. Furthermore, the energy eigenvectors are not orthogonal due to a non-Hermitian gauge field emerging near the exceptional points [5]. However, despite the progress in understanding the momentum-space structure of the polariton eigenenergies resulting from non-Hermiticity, a comprehensive understanding of the non-Hermitian dynamics in these experimentally relevant systems is still lacking, with the majority of studies focusing on the lattice models [24–26].

In this work, we investigate the non-Hermitian wave-packet dynamics in a microcavity polariton system using a two-band model relevant to the recent experiments [5] and focusing on observable effects. Apart from the previously predicted [16] motion in the absence of an external force, we also find that for some initial conditions, the wave packets tend to split into multiple components that propagate towards different directions. Moreover, these wave packets tend to evolve into different eigenstates and propagate towards the maxima of the imaginary part of the corresponding eigenenergy. We further show that this nonconservative dynamics of the wave-packet COM is accurately captured by the non-Hermitian extension of the Ehrenfest theorem, where the non-Hermitian

*eliezer.estrecho@anu.edu.au

component of the Hamiltonian drives the effective force field. Finally, we examine the polariton pseudospin textures resulting from the wave-packet evolution and describe the emergent pseudospin antimerons [29–34] on the imaginary Fermi arc in momentum space. Their detection on the imaginary Fermi arc would signify a clear signature of the non-Hermitian wave-packet dynamics.

This work is organized as follows. In Sec. II, we present the non-Hermitian polariton model considered in this work. In Sec. III A, we discuss the wave-packet self-acceleration and splitting in momentum space. In Sec. III B, we describe the asymptotic behavior of the polariton wave packets in momentum space and the unidirectional propagation in real space. Finally, in Sec. III C, we present our investigation of the dynamics of the polariton pseudospins, including the formation of the pseudospin defects on the imaginary Fermi arc without (Sec. III C 1) and with (Sec. III C 2) the presence of an out-of-plane field, and the formation of the defects in real space (Sec. III C 3). The discussion of the feasibility of experimental observation of the pseudospin defects and the analysis of wave-packet trajectories in other two-band systems (non-Hermitian Dirac model and the non-Hermitian Chern insulator) are presented in the Appendixes.

II. THEORETICAL MODEL

In this work, we consider polaritons under the influence of X - Y linear polarization splitting (optical anisotropy), and transverse-electric and transverse-magnetic (TE-TM) splitting (photonic spin-orbit coupling) [35]. Figure 1(a) schematically shows the planar microcavity containing an active material hosting the excitons that hybridize with the cavity photons to form polaritons. The anisotropy can arise from the birefringence of the cavity spacer or active material while the TE-TM splitting is naturally present in planar microcavities.

The complex dispersion, the momentum dependence of energy (real part) and linewidth (imaginary part) of anisotropic polaritons, can be modeled by a two-band non-Hermitian Hamiltonian $\mathbf{H}(\mathbf{k}) = H_0(\mathbf{k})\mathbf{I} + \vec{\mathbf{G}}(\mathbf{k}) \cdot \vec{\sigma}$, where $\vec{\mathbf{G}}(\mathbf{k}) = [G_x(\mathbf{k}), G_y(\mathbf{k}), G_z(\mathbf{k})]$ is the effective magnetic field arising from the X - Y and TE-TM splittings. Here, $\vec{\sigma}$ is a vector of Pauli matrices, \mathbf{I} is the 2×2 identity matrix, and $\mathbf{k} = (k_x, k_y)$ is the in-plane momentum.

The Hamiltonian is written in the basis of circular polarization of the cavity photon or the spin projection of the excitons on the z direction normal to the plane of the microcavity. This basis forms the canonical representation of the polariton pseudospin [36] (see Appendix B for details).

The specific Hamiltonian, valid for small momenta, has the following components [5,37]:

$$H_0(\mathbf{k}) = E_0 + \frac{\hbar^2 k^2}{2m} - i\gamma_0 - i\gamma_2 k^2 - i\gamma_4 k^4, \quad (1)$$

$$\vec{\mathbf{G}}(\mathbf{k}) = [\tilde{\alpha} + \tilde{\beta}(k_x^2 - k_y^2), 2k_x k_y \tilde{\beta}, \Delta_z].$$

Dropping the k dependence for brevity, the expression for the complex energy can be written as $E_{\pm} = H_0 \pm G$, where $G = \sqrt{\vec{\mathbf{G}} \cdot \vec{\mathbf{G}}}$. The typical complex dispersion of the lower polariton branch probed in the experiments (see, e.g., Ref. [5]) is presented in Figs. 1(b) and 1(c).

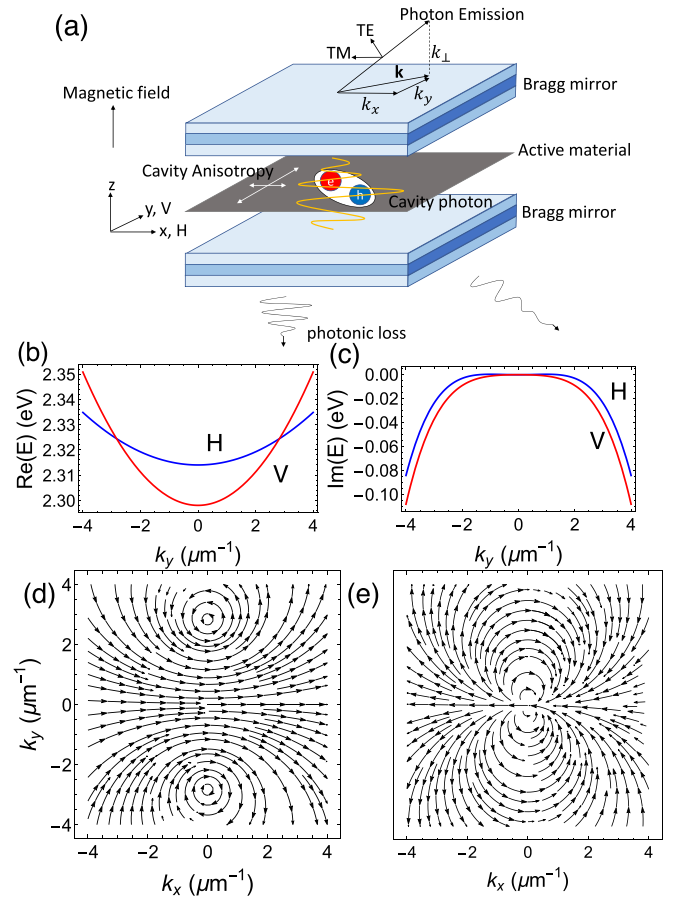


FIG. 1. (a) Schematic of the microcavity structure hosting anisotropic polaritons made by sandwiching an active material hosting excitons (electron-hole pair) between two Bragg mirrors. The anisotropy axis is aligned to either the x or y direction of the laboratory frame. The linearly polarized modes V, H, TE, and TM are defined accordingly. The momentum $\hbar\mathbf{k}$ of the polaritons is the in-plane component of the momentum of the emitted photon. (b),(c) Splitting of the energies and the linewidths of H and V polarized polariton modes due to anisotropy and TE-TM splitting at $k_x = 0$. (d),(e) In-plane vector plot of the (d) real and (e) imaginary parts of the effective magnetic field $\vec{\mathbf{G}}(\mathbf{k})$ when the Zeeman splitting is zero. If $\Delta_z \neq 0$, $\text{Re} \vec{\mathbf{G}}$ will have a constant out-of-plane component. The parameter values used here and in the rest of the text are listed in Appendix A.

The terms $E_0 + \hbar^2 k^2 / 2m$ describe the typical polariton dispersion, without polarization splitting, where E_0 is the energy of the lower polariton branch at zero momentum and m is its effective mass. The polarization-independent loss terms $-i\gamma_0 - i\gamma_2 k^2 - i\gamma_4 k^4$ arise from the nonmonotonous momentum dependence of the mean polariton linewidth, as illustrated by the polynomial fitting of the data in Ref. [5]. This ensures that the imaginary parts of the eigenenergies $\text{Im} E_{\pm}$ are always negative since this model describes the effects of both gain (e.g., an optical pump) and loss (e.g., radiative decay) by an effective loss term that determines the linewidth of the polariton spectrum. Positive values of $\text{Im} E_{\pm}$ would suggest a net gain, which is not physical for this system. The fourth-order term in the polynomial expansion is necessary to capture

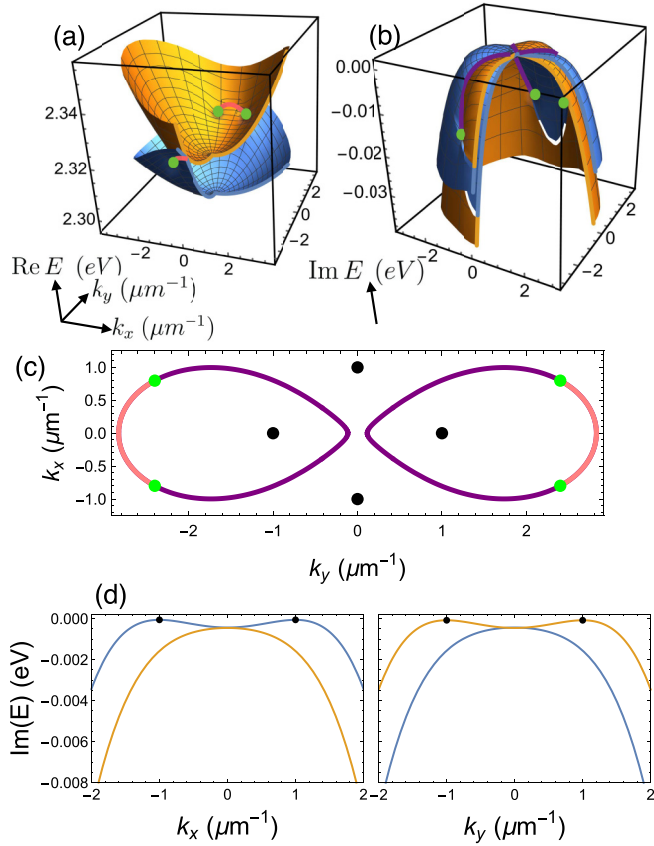


FIG. 2. The (a) real and (b) imaginary parts of the polariton eigenenergies with cuts to show the degeneracies. Green dots mark the exceptional points, and the pink and purple arcs are guides to the eye indicating the bulk and the imaginary Fermi arcs, respectively. (c) The momentum-space structure of the bulk Fermi arcs, the imaginary Fermi arcs, and the exceptional points shown in (a) and (b). (d),(e) The imaginary parts of the eigenenergies $\text{Im} E_+$ (orange line) and $\text{Im} E_-$ (blue line) at $k_y = 0$ and $k_x = 0$, respectively. The black dots mark the maxima of $\text{Im} E_{\pm}$.

the nonmonotonic behavior of the linewidths even at low momenta. This effect can arise from the coupling of excitons with near-constant linewidth and cavity photons with strongly k -dependent linewidth, and was experimentally observed in Ref. [5], where the local minima of the linewidth (or maxima of $\text{Im} E$) have occurred at a finite k .

The polarization-dependent terms in Eq. (1) are captured by \vec{G} , where $\tilde{\alpha} = \alpha - ia$ captures the effect of anisotropy which leads to both energy and linewidth splitting between the linearly polarized horizontal (H) and vertical (V) modes, and $\tilde{\beta} = \beta - ib$ describes the photonic spin-orbit coupling which splits the transverse electric (TE) and transverse magnetic (TM) polarization modes [5]. This is the non-Hermitian generalization of the model presented in Ref. [37]. The Δ_z term describes the effects of Zeeman splitting induced by an out-of-plane magnetic field which can be introduced externally [38]. The in-plane real and imaginary components of the effective field \vec{G} are presented in Figs. 1(d) and 1(e).

The eigenenergies of the polariton Hamiltonian (1) E_{\pm} are plotted in Figs. 2(a) and 2(b). The two polariton energy bands

exhibit two pairs of exceptional points (spectral degeneracies) located at

$$k^{EP} = \sqrt{\frac{\alpha - ia}{\beta - ib}},$$

$$\phi^{EP} = \pm \frac{\pi}{2} \pm \arg \sqrt{\frac{\alpha - ia}{\beta - ib}}, \quad (2)$$

where $[k_x, k_y] = [k \cos \phi, k \sin \phi]$ when $\Delta_z = 0$. The exceptional points in each pair are connected by the bulk Fermi arc where the real energy surfaces cross, and by the imaginary Fermi arc where the imaginary energy surfaces cross [see Figs. 2(a)–2(c)] [5,39]. A nonzero Zeeman splitting Δ_z would shrink the bulk Fermi arc, moving the exceptional points in a pair towards each other such that when $|\Delta_z| > |(a\beta - b\alpha)/\beta|$, the exceptional points annihilate and open a gap.

As shown in Fig. 2(b) and highlighted in Figs. 2(d) and 2(e), $\text{Im} E_+$ has two maxima lying on the k_y axis, while $\text{Im} E_-$ has two maxima at the k_x axis. These points play an important role in the dynamics of the polariton wave packets, as discussed in the next section.

Note that the orientation of the exceptional points and the local maxima of $\text{Im} E_{\pm}$ depends on the orientation of the birefringence, i.e., of the sample with respect to the laboratory frame. The orientation chosen here is determined by the choice of parameters in the model given by Eq. (1).

III. RESULTS AND DISCUSSION

To understand the influence of the non-Hermiticity on the dynamics of anisotropic polaritons, inspired by previous works [16,17], we investigate the dynamics of Gaussian wave packets in the polariton system described by the model Hamiltonian (1). Since the Hamiltonian contains k components only and no external potential, the time evolution of wave packets in real and momentum spaces and the resulting pseudospin textures can be exactly calculated (see Appendix C for details).

The initial Gaussian wave packet is a superposition of multiple \mathbf{k} components of the pseudospin eigenstates, whose individual contributions to the time evolution can be described by

$$|\psi_{\pm}^R(\mathbf{k}, t)\rangle = e^{-i \text{Re} E_{\pm}(\mathbf{k})t} e^{\text{Im} E_{\pm}(\mathbf{k})t} |\psi_{\pm}^R(\mathbf{k})\rangle, \quad (3)$$

where the superscript R denotes the right eigenstates (see Appendix D for details). The variation in the imaginary part, as shown below, is responsible for the peculiar effects described in this work.

The COM in real and momentum spaces are then calculated using the expectation values of k and x following previous work [17] as follows:

$$\langle \mathbf{k}(t) \rangle = \frac{\int \langle \psi(\mathbf{k}, t) | \mathbf{k} | \psi(\mathbf{k}, t) \rangle d^2 \mathbf{k}}{\int \langle \psi(\mathbf{k}, t) | \psi(\mathbf{k}, t) \rangle d^2 \mathbf{k}},$$

$$\langle \mathbf{x}(t) \rangle = \frac{\int \langle \psi(\mathbf{x}, t) | \mathbf{x} | \psi(\mathbf{x}, t) \rangle d^2 \mathbf{x}}{\int \langle \psi(\mathbf{x}, t) | \psi(\mathbf{x}, t) \rangle d^2 \mathbf{x}}. \quad (4)$$

This ensures that even though the time evolution is nonunitary, we can still normalize the wave function at each point in

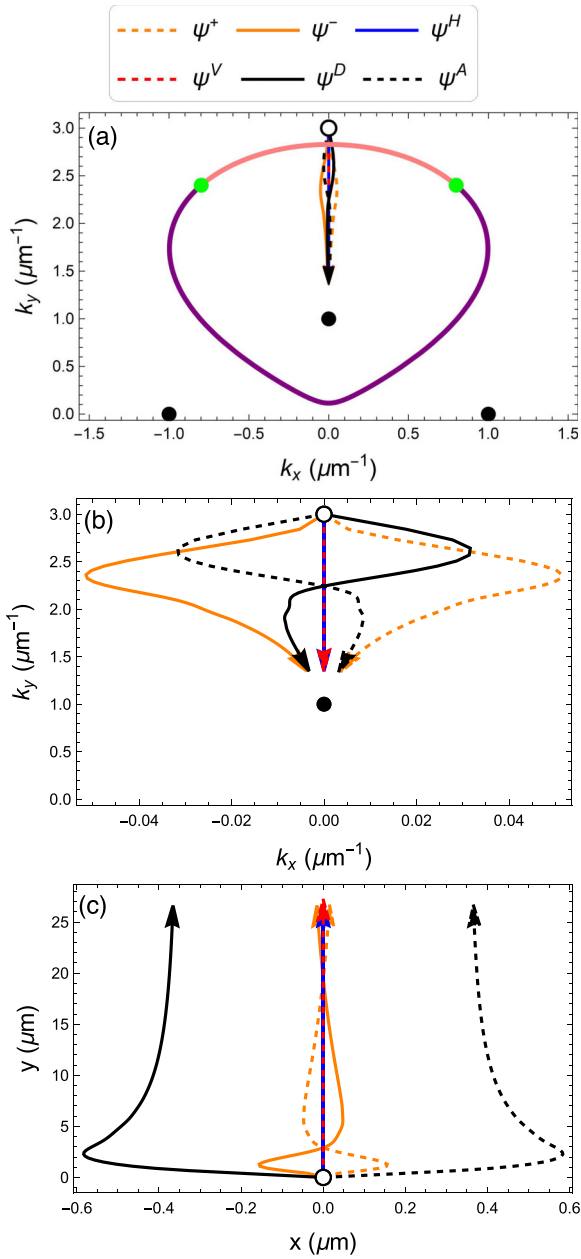


FIG. 3. The polarization-dependent trajectories of the COM of the polariton wave packet in (a), (b) the momentum space and (c) the real space, where (b) is the zoom-in of (a). Note that the trajectories of the horizontally polarized and the vertically polarized modes overlap. The open dots denote the initial wave-packet center of mass in both momentum and real space and the black dots denote the maxima of $\text{Im} E_{\pm}$ in momentum space.

time. These two quantities can be experimentally measured in polariton systems since we have access to the distribution of the polaritons in both real and momentum spaces.

A. Self-acceleration and splitting of wave packets

Example COM trajectories of the wave packets in real and momentum spaces are presented in Fig. 3, which clearly shows the accelerating behavior in the absence of an external field. The same self-acceleration was previously observed in

other non-Hermitian systems [16,17]. Furthermore, the trajectories are sensitive to the polarization of the initial wave packet. However, regardless of the initial polarization, the self-accelerating wave packets tend to move towards the same point in momentum space or towards the same direction in real space. This point in momentum space, which we denote \mathbf{k}^* , corresponds to the maximum of the imaginary part of the eigenenergy.

Intuitively, the acceleration arises from the gradient of the imaginary part of eigenenergy $\nabla \text{Im} E_{\pm}$ [see Figs. 2(b), 2(d), and 2(e)] [16]. Some k components are decaying faster than others, causing the wave packet to reshape and resulting in an effective displacement of the COM towards k components with larger imaginary part (or lesser decay rates), until it reaches the value of k^* . However, the actual trajectory of the wave packet does not follow $\nabla \text{Im} E_{\pm}$, as we show here and in other two-band systems (see Appendix F).

The acceleration of the wave packet can be derived from the Ehrenfest theorem [40]. In Hermitian systems, the wave packet will accelerate when the Hamiltonian is either time dependent or does not commute with the momentum operator, e.g., when H has spatial dependence. Our Hamiltonian, given by Eq. (1), satisfies neither of these conditions. However, extending Ehrenfest theorem to our system [41,42] leads to the following equation of motion:

$$\frac{d}{dt} \langle \mathbf{k} \rangle = \frac{i}{\hbar} \langle \mathbf{k} H_n \rangle - \frac{i}{\hbar} \langle \mathbf{k} \rangle \langle H_n \rangle, \quad (5)$$

where $H_n = H^{\dagger} - H$ is the non-Hermitian component of the Hamiltonian, the imaginary parts of H_0 and \vec{G} . The extended Ehrenfest theorem clearly shows that the observed self-acceleration is due to the non-Hermitian terms.

If the initial polarization of the wave packet is the right eigenstate $|\psi_{\pm}^R\rangle$, Eq. (5) can be further simplified as

$$\frac{d}{dt} \langle \mathbf{k} \rangle = \frac{2}{\hbar} \langle \mathbf{k} \text{Im} E_{\pm} \rangle - \frac{2}{\hbar} \langle \mathbf{k} \rangle \langle \text{Im} E_{\pm} \rangle. \quad (6)$$

This expression highlights that the self-acceleration results from the imaginary parts of the eigenenergies. Moreover, we note that when $\text{Im} E_{\pm}$ are constants, the two terms in Eq. (6) will cancel out. Hence, a nonzero gradient of $\text{Im} E_{\pm}$ is necessary for the self-acceleration.

Note that the self-acceleration arising from Eq. (5) also depends on the current state of the system. Therefore, the dynamics of $\langle \mathbf{k} \rangle$ depends on the COM momentum, width, and polarization of the wave packet, as well as time. This explains the previous findings that wave packets with larger widths in momentum space show larger accelerations [16] and the polarization-dependent trajectories in Fig. 3 (see, also, Ref. [16]).

Although Eq. (5) describes complicated dynamics, its right-hand side defines an effective k -dependent force field corresponding to the self-acceleration of an initial wave packet. Two examples of the initial force fields, denoted as $d_i \langle \mathbf{k} \rangle$, are presented in Figs. 4(a) and 4(b), where the fields are calculated for a fixed-width Gaussian wave packet centered at \mathbf{k} with initial horizontal or vertical polarizations, respectively. The H-polarized wave packets tend to accelerate towards two of \mathbf{k}^* at $\mathbf{k} = (0, \pm 1) \mu\text{m}^{-1}$ [see Fig. 4(a)], while the V-polarized one tends towards the other $\mathbf{k} = (\pm 1, 0) \mu\text{m}^{-1}$

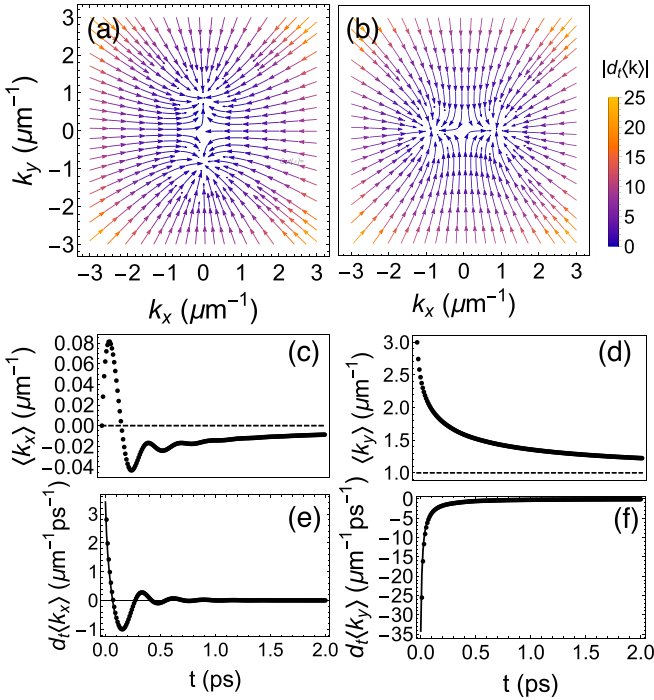


FIG. 4. The time derivative of the COM momenta $d_t(\mathbf{k})$ of (a) horizontally polarized and (b) vertically polarized wave packets with different initial COM momenta \mathbf{k}_0 at $t = 0$ ps, respectively. (c),(d) The COM momenta of an initially diagonally polarized wave packet, initially centered at $\mathbf{k}_0 = (0, 3)$, while the dotted lines denote \mathbf{k}^* . (e),(f) $d_t(\mathbf{k})$ of same wave packet. The black lines are $d_t(\mathbf{k})$ calculated from Eq. (5), which fully agree with the numerical results (black dots).

[see Fig. 4(b)]. This reflects the results presented in Fig. 3 in which the magnitude of the acceleration is minimized around \mathbf{k}^* .

The force field also changes with time as the momentum distribution and polarization evolve. An example is presented in Figs. 4(c)–4(f) for the D-polarized initial wave packet in Fig. 3. The acceleration of the wave packet oscillates and decays to zero as the wave packet propagates towards $\mathbf{k}^* = (0, 1) \mu\text{m}^{-1}$. The agreement between the acceleration calculated from the direct simulation (dots) and from Eq. (5) (line) clearly shows that the non-Hermitian extension Ehrenfest theorem accurately captures the COM dynamics, and therefore provides a semiclassical description of the wave-packet dynamics.

Note that the effective force field is distinct from the real and imaginary parts of the effective magnetic field [see Figs. 1(d) and 1(e)] and from the gradient of the imaginary part of E_{\pm} , $\nabla \text{Im} E_{\pm}$.

Surprisingly, when the wave packet is initialized on the imaginary Fermi arc, it splits into two components that propagate away from each other, as seen in Figs. 5(a)–5(c). Furthermore, when the wave packet is initialized at the origin $\mathbf{k} = 0$, while overlapping with the two imaginary Fermi arcs, it splits into four components that accelerate away from each other along the $\pm k_x$ and $\pm k_y$ directions [see Figs. 5(d)–5(f)].

The splitting of the wave packets is due to the different imaginary parts (or decay rates) of the two eigenstates. It

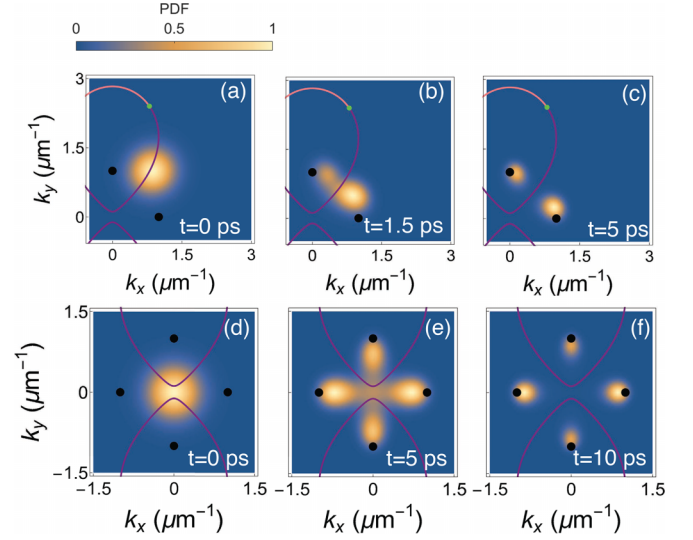


FIG. 5. Splitting of the exciton-polariton wave packet when initialized (a)–(c) on the imaginary Fermi arc and (d)–(f) at the origin. The black dots denote \mathbf{k}^* . The plots and the colorbar represent the evolution of the normalized probability density function (PDF). Note that this is not equal to the wave-packet amplitude $|\psi|^2$, which decreases over time due to the continuous decay.

is natural for the wave packet to evolve with time towards an eigenstate with the larger growth rate (or the smaller decay rate). In our model, $\text{Im} E_+(\mathbf{k})$ is larger inside the region bounded by the Fermi arcs, while $\text{Im} E_-(\mathbf{k})$ is larger outside. Therefore, the components of the wave packets bounded by the Fermi arcs will evolve towards the upper eigenstate $|\psi_+^R(\mathbf{k})\rangle$, while those outside the region will evolve towards the lower eigenstate $|\psi_-^R(\mathbf{k})\rangle$. Hence, the wave packet splits, as shown in Fig. 5.

This analysis is supported by the time evolution of the normalized components of the upper and lower eigenstates shown in Fig. 6, corresponding to the case presented in Figs. 5(a)–5(c). One component quickly becomes dominant such that the components inside (outside) the region bounded by the Fermi arcs belong to the upper (lower) eigenstate. The situation is the same for the case presented in Figs. 5(d)–5(f). Note that since the difference in the imaginary parts of the two eigenenergies, $\text{Im}(\Delta E)$, is larger for large k (see Fig. 2), the components of the wave packets with large k will evolve into the two eigenstates faster than the components near $\mathbf{k} = 0$.

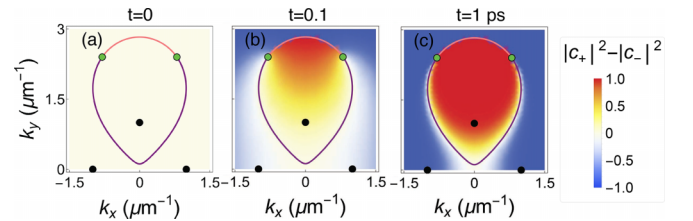


FIG. 6. (a)–(c) Evolution of the wave packet initially prepared as an equal superposition of the two eigenstates $|\psi\rangle = c_+|\psi_+^R\rangle + c_-|\psi_-^R\rangle$ (see Appendix D for details). Shown is $(|c_+|^2 - |c_-|^2) / (|c_+|^2 + |c_-|^2)$. The green dots denote the exceptional points and the black dots denote \mathbf{k}^* .

Importantly, whenever the wave packets split, the extended Ehrenfest theorem fails to capture their motion as the COM momenta will no longer correspond to the peak of the wave packets.

B. Directional propagation of wave packets

After the wave packet evolves into the eigenstates with the larger $\text{Im} E$, its COM will then propagate towards the maxima of the corresponding $\text{Im} E$ in momentum space, as shown in Figs. 5(c) and 5(f). In real space, the wave packets will asymptotically exhibit directional transport with a group velocity corresponding to the $\nabla_{\mathbf{k}} \text{Re} E$ at \mathbf{k}^* [17].

In our model, $\text{Im} E_+$ has two maxima at $(0, \pm k_+^*)$ inside the region bounded by the Fermi arcs, while $\text{Im} E_-$ has two maxima at $(\pm k_-^*, 0)$ outside this region [see Fig. 2(c)]. Hence, wave packets inside the region bounded by the Fermi arcs will asymptotically reach the points $\mathbf{k}^* = (0, \pm k_+^*)$ while those outside this region reach $\mathbf{k}^* = (\pm k_-^*, 0)$. Note that for $\Delta_z = 0$, we have $k_{\pm}^* = \sqrt{(\gamma_2 + b)/2\gamma_4}$.

In real space, the wave packets asymptotically reach their corresponding nonvanishing group velocities. The wave packets inside the Fermi arcs will have $\langle \mathbf{v}_+ \rangle = (0, \pm v_+^*)$, while those outside will have $\langle \mathbf{v}_- \rangle = (\pm v_-^*, 0)$, where (for $\Delta_z = 0$)

$$v_{\pm}^* = \left(\frac{\hbar}{2m} - \frac{\beta}{\hbar} \right) \sqrt{\frac{2(\gamma_2 + b)}{\gamma_4}}. \quad (7)$$

Note that these asymptotic group velocities of the wave packets only depend on the mean linewidth parameters $\gamma_{2,4}$, and the spin-orbit coupling parameters β and b . The anisotropy, however, determines the direction.

In the limit of a tightly focused wave packet in real space, hence covering multiple \mathbf{k}^* in momentum space, the wave packet will split into four parts, with each part funneling to the vicinity of \mathbf{k}^* that it covered, as shown in Figs. 7(a)–7(c). In real space, the wave packet splits and spreads over time, eventually evolving into four broad wave packets in the two eigenstates. Each of the smaller wave packets exhibits directional transport with the corresponding nonvanishing asymptotic group velocities $\langle \mathbf{v}_{\pm} \rangle$ [see Figs. 7(a)–7(f)].

In the presence of Zeeman splitting, i.e., $\Delta_z \neq 0$, the \mathbf{k}^* points can be found numerically. Increasing Δ_z will move them towards $\mathbf{k} = 0$ [see Figs. 7(g) and 7(h)]. Since the \mathbf{k}^* points stay on the k_x and k_y axes, Δ_z will only change the magnitude of the final group velocities, but not the directions. The final group velocities depend on Δ_z nonmonotonically, as seen in Figs. 7(i) and 7(j).

Note that when the system is isotropic, both α and a vanish and the exceptional points will move to the origin and merge into a single Hermitian-like degeneracy with two distinct eigenstates. In this case, the four maxima at \mathbf{k}^* will join to form a ring around the origin with radius $k = \sqrt{(\gamma_2 + b)/2\gamma_4}$. Hence, the wave packet will propagate and evolve towards this ring.

It is worth mentioning that the above results are derived under the assumption that the polariton wave packet is initialized as a superposition of the two eigenstates, $|\psi\rangle = c_+|\psi_+^R\rangle + c_-|\psi_-^R\rangle$, which have nonzero $|c_{\pm}|$ at all of \mathbf{k}^* . In contrast, if the initial state is in one of the eigenstate $|\psi_{\pm}^R\rangle$, the wave packet

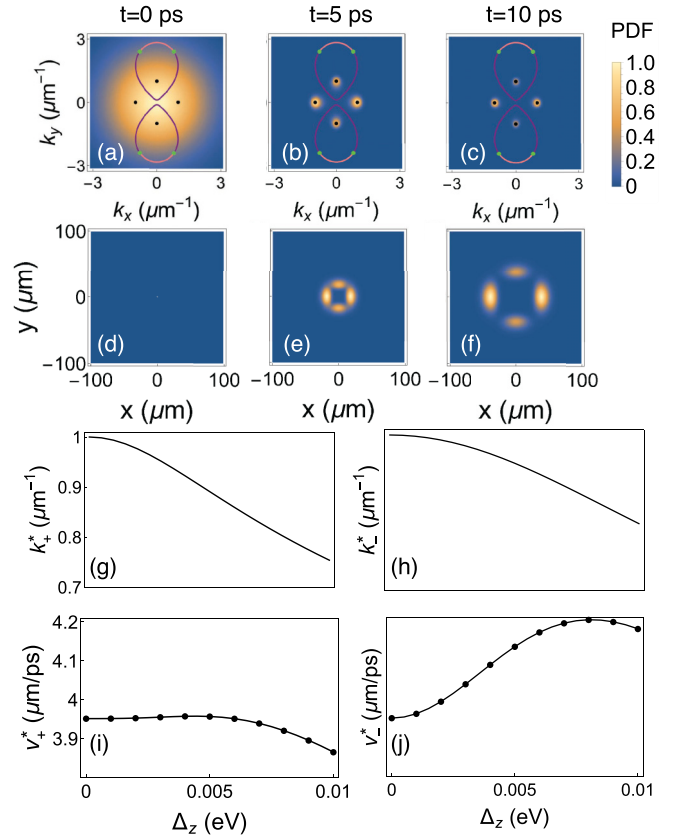


FIG. 7. (a)–(c) Momentum-space and (d)–(f) real-space time evolution of a spatially tightly focused initial wave packet. (g),(h) Coordinates of the \mathbf{k}^* points as a function of Zeeman splitting Δ_z , where $\mathbf{k}^* = (0, \pm k_+^*)$, $(\pm k_-^*, 0)$. (i),(j) Asymptotic group velocities where $\langle \mathbf{v}_+ \rangle = (0, \pm v_+^*)$ and $\langle \mathbf{v}_- \rangle = (\pm v_-^*, 0)$. The black lines in (i) and (j) represent the group velocities $\mathbf{v} = \nabla_{\mathbf{k}} \text{Re} E_{\pm}$ calculated from \mathbf{k}^* in (g) and (h), which show excellent agreement with the results from the numerical simulation of wave-packet dynamics (black dots).

will only propagate towards the corresponding $\max(\text{Im} E_{\pm})$. Furthermore, if the components of the eigenstate $|c_{\pm}|^2$ in the initial state are zero at the corresponding $\max(\text{Im} E_{\pm})$, the wave packets will not asymptotically funnel to $\max(\text{Im} E_{\pm})$.

For example, when $\Delta_z = 0$, the upper eigenstate at the points $\mathbf{k}^* = (0, \pm k_+^*)$ inside the region bounded by the Fermi arcs is H polarized. Therefore, if the initial state is V polarized and has no H component, the polaritons at $\mathbf{k}^* = (0, \pm k_+^*)$ cannot evolve into $|\psi_+^R\rangle$, as shown in Figs. 8(a)–8(c). Consequently, the wave packet will never funnel to the corresponding \mathbf{k}^* points [see Figs. 8(d)–8(f)]. Instead, the wave packet will funnel to the other extrema at $\mathbf{k}^* = (\pm k_-^*, 0)$ and exhibit directional transport in real space at the constant velocities $\langle \mathbf{v}_- \rangle$. This also explains why the extended Ehrenfest theorem predicts $d_t \langle \mathbf{k} \rangle \approx 0$ only at $\mathbf{k}^* = (\pm k_-^*, 0)$ [or $\mathbf{k}^* = (0, \pm k_+^*)$] for the V-polarized [or H-polarized] wave packets in Figs. 4(a) and 4(b).

C. Dynamics of exciton-polariton pseudospin textures

The self-acceleration of the polariton wave packets is accompanied by nontrivial pseudospin dynamics. The polariton pseudospin can be characterized by the Stokes vector

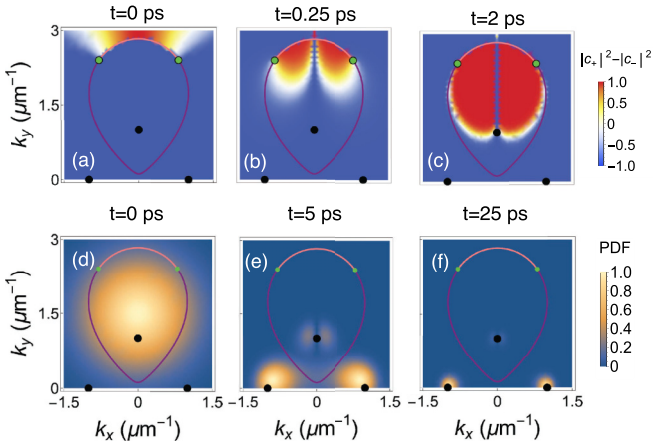


FIG. 8. (a)–(c) Time evolution of $(|c_+|^2 - |c_-|^2)/(|c_+|^2 + |c_-|^2)$ when the initial wave packet is vertically polarized. (d)–(f) Time evolution of the wave packet with black dots marking $\mathbf{k}^* = \max(\text{Im } E_{\pm})$ and green dots marking the exceptional points.

$\mathbf{S} = [S_x, S_y, S_z]$ as defined in Appendix B and the corresponding pseudospin distributions in momentum space can be characterized using the analogy with electronic spin textures [29–32,43,44]. As described in the previous section, the polariton wave packets tend to evolve into different eigenstates in different regions in momentum space. Since these regions are separated by the Fermi arcs, it is natural to investigate what happens close to these arcs. As shown in Figs. 9(a) and 9(b), the pseudospin textures of the two eigenstates have opposing in-plane components but the same out-of-plane components [5]. While the pseudospin texture of each eigenstate is antiparallel on both sides of the bulk Fermi arc, it can transition smoothly to the texture of the other eigenstate. On the other hand, the pseudospin textures of both eigenstates are continuous across the imaginary Fermi arcs.

In the following, we study the dynamics of the pseudospin texture as the polariton wave packets self-accelerate, split, and evolve into different eigenstates. We observe the emergence of pseudospin defects as presented in Figs. 9(c)–9(h). The evolution of the pseudospin textures and the emergence of the defects depend only on the initial polarization of the wave packet, and not on the spatial or momentum components. Therefore, the pseudospin textures can evolve independently from the probability density function of the wave packet. Therefore, the defects can be generated even in the regions not covered by the bulk of the wave packet in momentum space.

1. Pseudospin defects

The pseudospin defects on the imaginary Fermi arcs are nonsingular point defects similar to skyrmions [29–33,43–48]. As the wave packet evolves, these defects first emerge at the segments of the imaginary Fermi arcs with large k , where the difference between the decay rates of the two bands, $\text{Im}(\Delta E)$, is the largest. Then, more defects are generated at segments with smaller k on the imaginary Fermi arc where $\text{Im}(\Delta E)$ is smaller. The defects then move towards the exceptional points along the imaginary Fermi arc. This results in the defects becoming more densely packed as more defects are generated.

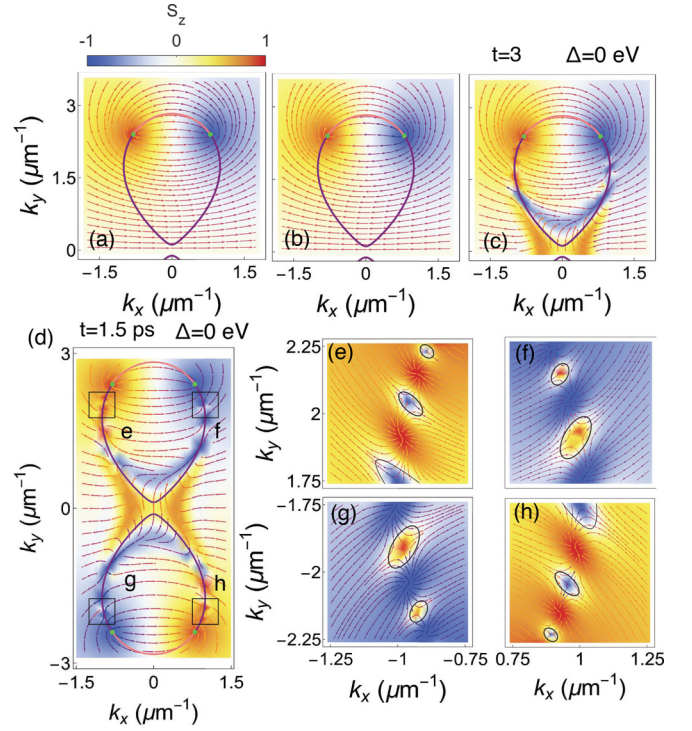


FIG. 9. The pseudospin textures of (a) the upper eigenstate, (b) the lower eigenstate, and (c) a polariton wave packet at $t = 3$ ps with $\Delta_z = 0$. (d) The pseudospin textures of the polariton wave packet at $t = 1.5$ ps. (e)–(h) Zoom-in of the areas marked in (d) near the pseudospin defects on the imaginary Fermi arcs. The color represents the directions of S_z , while the arrows represent the in-plane pseudospins (S_x, S_y) .

Topological point defects can be characterized by a winding number called the skyrmion number, N_{sk} , which counts how many times the pseudospin wraps around the unit sphere [29–31],

$$N_{sk} = \frac{1}{4\pi} \iint \mathbf{S} \cdot (\partial_x \mathbf{S} \times \partial_y \mathbf{S}) d^2 \mathbf{r}. \quad (8)$$

The skyrmion number can also be expressed in terms of two other topological invariants, i.e., the vorticity w and the polarity p , as $N_{sk} = wp/2$. The vorticity measures the in-plane winding of \mathbf{S} along a curve encircling the core counterclockwise [31,33,34,49], while the polarity measures the out-of-plane winding of \mathbf{S} and quantifies the continuous change of S_z from the center to the edge of the defect [31,33,34,46,47,49].

Skyrmions exhibit both in-plane and out-of-plane winding. The in-plane Stokes vectors of a skyrmion are similar to that of a spin vortex, resulting in a vorticity of $w = +1$. Furthermore, a core-up (core-down) skyrmion has an out-of-plane Stokes vector $S_z = +1$ ($S_z = -1$) at the center, which continuously transforms into $S_z = -1$ ($S_z = +1$) at the edge, giving it a polarity of $p = +2$ ($p = -2$) [29–33,43–47]. Consequently, a core-up (core-down) skyrmion has a skyrmion number of $N_{sk} = +1$ ($N_{sk} = -1$). Similarly, an antiskyrmion has in-plane Stokes vectors $[S_x, S_y]$ similar to the ones in an antivortex and a core-up (core-down) antiskyrmion has a

polarity of $p = +2$ ($p = -2$), giving it a skyrmion number of $N_{sk} = -1$ ($N_{sk} = +1$) [31].

The pseudospin defects that we observe [see Figs. 9(d)–9(h)] are core-up and core-down defects, but with $S_z = 0$ at the edges. These defects have vorticities of $w = -1$ and the z components of their pseudospins perform a $\pi/2$ rotation instead of a π rotation [29], and thus have polarities $p = +1$ ($p = -1$). Hence, these defects have skyrmion numbers $N_{sk} = -1/2$ ($N_{sk} = +1/2$). We, therefore, conclude that these defects are core-up and core-down antimerons, i.e., antiskyrmions with half-integer winding numbers.

In the vicinity of the exceptional points in the upper-half plane ($k_y \geq 0$), core-up and core-down antimerons form on the right-hand side ($k_x \geq 0$) and left-hand side ($k_x \leq 0$) of the exceptional points pair, respectively. On the lower-half plane, the configuration is flipped. It is interesting to note that this configuration is consistent with the configuration of the spectral winding around the exceptional points in this system [5].

We also observe pseudospin vortices with core polarization $S_z = +1$ ($S_z = -1$) forming between the core-down (core-up) antimerons on the imaginary Fermi arcs [see Figs. 9(d)–9(h)]. The in-plane pseudospins wind around the vortex cores, giving them vorticities of $w = +1$. However, the $S_z = \pm 1$ at their cores does not transform into $S_z = \mp 1$ or $S_z = 0$ on the edge. Consequently, they do not have $p = \pm 2$ like a skyrmion or $p = \pm 1$ like a meron, and therefore do not have integer-valued or half-integer-valued skyrmion numbers.

2. Pseudospin defects with Zeeman splitting

Although the Zeeman splitting Δ_z will not drastically change the in-plane textures $[S_x, S_y]$ of the defects, it has a huge impact on the S_z textures of the eigenstates and the defects. As Δ_z increases, one eigenstate gains more positive S_z component, while the other eigenstate gains the component of the opposite sign. As shown in Fig. 10, S_z becomes more negative on one side of the imaginary Fermi arc, and more positive on the other side with increasing $|\Delta_z|$. Consequently, some of the defects slightly drift away from the imaginary Fermi arcs.

Which defects are pushed away from the imaginary Fermi arcs depends on the initial polarization of the wave packet and the sign of the Zeeman splitting Δ_z . For example, for an initially circularly polarized wave packet, ψ^+ , the core-up antimerons and vortices stay on the imaginary Fermi arcs. The core-down defects drift outward (inward) of the region bounded by the Fermi arcs [see Figs. 10(a)–10(c)] for positive Δ_z as they gain more negative (positive) S_z in this region [see also Figs. 10(d)–10(f) for the negative Δ_z case]. If the wave packet initially has the opposite polarization, ψ^- , the opposite happens, and the core-down defects would stay on the arc while the core-up defects drift away.

Another consequence of the Zeeman splitting is that the core-up and core-down defects also gain more positive and negative S_z contribution, respectively. If $|\Delta_z|$ continues to increase, eventually the pseudospin on the edge of the antimerons will no longer lie on the xy plane. Consequently, S_z in these defects will no longer perform $\pi/2$ rotations

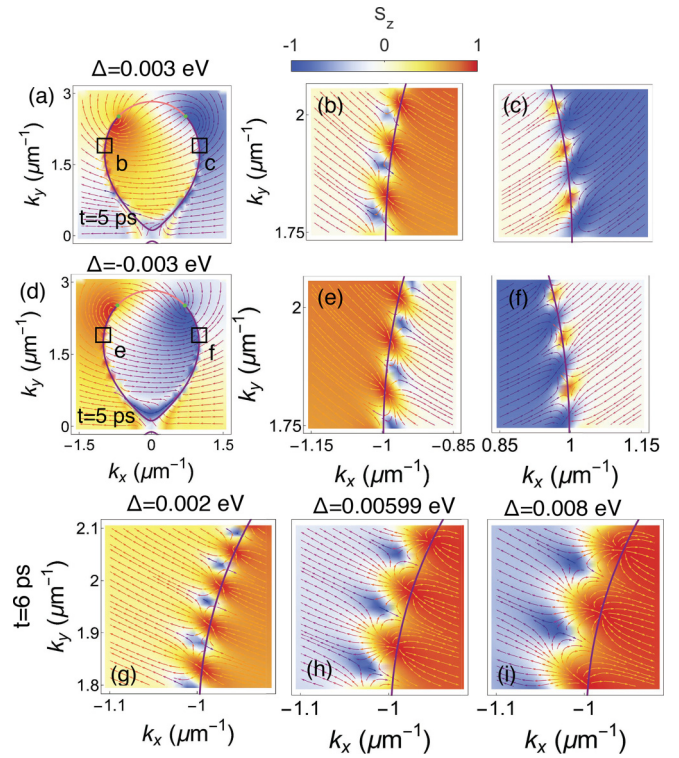


FIG. 10. Pseudospin textures for (a)–(c) positive and (d)–(f) negative values of Zeeman splitting showing how the core-down defects drift away from the imaginary Fermi arc. (g)–(i) Textures in the (g) gapless phase with nonzero Δ_z , (h) the phase where the two exceptional points merge, and (i) the gapped phase. The wave packets are initially circularly polarized.

with respects to the xy plane, and they lose their antimeron character [see Figs. 10(g)–10(i)]. This is different from the self-acceleration, splitting, and directional transport of the wave packets, which can persist at large $|\Delta|$.

3. Pseudospin defects in real space

The pseudospin antimerons on the imaginary Fermi arc in momentum space can also be seen in the real space. When the wave packet covers the antimerons in momentum space, the antimeron textures also emerge in the real space (see Fig. 11). The emergence of these antimerons is a direct consequence of the antiparallel pseudospins on the imaginary Fermi arc as the wave packet evolves into different eigenstates. This is in contrast to the previous studies of purely Hermitian two-dimensional systems, where the topological defects emerge due to the cavity anisotropy and TE-TM splitting [29,34,43,50].

Our results show a different way to generate topological defects in the pseudospin structures that arise from the growth and decay of wave packets in a non-Hermitian system. These defects also represent a clear signature of the effects of the imaginary Fermi arc on polariton dynamics in the real space. Moreover, our preliminary estimates indicate that these defects can be observed experimentally in a polariton system based, for example, on a perovskite embedded in a high-quality microcavity [5] (see Appendix E).

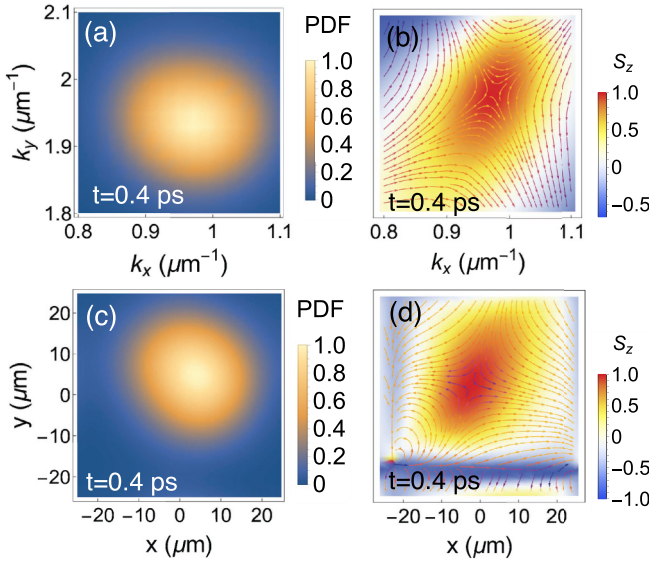


FIG. 11. An exciton-polariton wave packet and its pseudospin textures in (a),(b) the momentum and (c),(d) the real space.

IV. CONCLUSION AND OUTLOOK

To conclude, we have investigated the dynamics of wave packets in a non-Hermitian exciton-polariton system. We found that the wave packets tend to evolve into the eigenstate with the larger imaginary part of the energy $\text{Im} E$, then propagate towards the momentum corresponding to the $\max(\text{Im} E)$. This results in splitting, self-acceleration, and directional transport of the wave packets in the absence of an external field. These effects arise from the imbalance of decay rates (or gain) between the eigenstates due to the non-Hermitian components of the Hamiltonian. We also show that the non-Hermitian extension of the Ehrenfest theorem results in a semiclassical equation of motion for non-Hermitian wave-packet dynamics.

We also observe the formation of core-up and core-down antimerons in momentum space on the imaginary Fermi arc during the propagation of the wave packets. Using realistic parameters, we predict that these defects can be observed in both momentum and real space. The origin of these pseudospin defects and their connections to the Fermi arcs as well as the spectral winding around the exceptional points require further investigation.

Although here we focus on polaritons, our results are general and applicable to other two-dimensional two-band systems, including purely photonic systems. However, experimentally, the coupling between photons and excitons results in a larger effective mass and slower propagation speeds, potentially allowing us to observe the predicted dynamics at a picosecond scale using a streak camera [51]. In addition, the presence of distinct extrema of the polariton linewidth at a finite momentum, which arises from photon-exciton coupling, is responsible for the interesting dynamics described in this work.

Our results shed light on the dynamics of wave packets and pseudospins in a polariton system, as well as related non-Hermitian systems. Furthermore, we believe that the emergent momentum-space antimeron textures will enable the direct

observation of the influence of the imaginary Fermi arcs on the dynamics of the system. All of the effects described above do not require an external potential and can be observed in a polariton system with optical anisotropy arising from the material properties of the semiconductor, e.g., perovskite [5] and the organics [27], or in a photonic cavity with an anisotropic spacer [28,52]. Our results highlight the excellent potential of polaritons as a platform to study non-Hermitian dynamics.

ACKNOWLEDGMENTS

We acknowledge support from the Australian Research Council (ARC) through the Centre of Excellence Grant No. CE170100039 and the Discovery Early Career Researcher Award No. DE220100712. Y.-M.R.H. is a recipient of Australian Government Research Training Program (RTP) Scholarship.

APPENDIX A: VALUES OF PARAMETERS

For the figures presented in this work, we chose the parameters such that the exceptional points are well separated and the bulk Fermi arcs are clearly visible. We set $\gamma_2 = 0 \mu\text{m}^2\text{eV}$, $\gamma_4 = 3.75 \times 10^{-4} \mu\text{m}^4\text{eV}$, and choose the mean energy, linewidth, and effective polariton mass to be $E_0 - i\gamma_0 = 2.306 - 4.5 \times 10^{-4}i\text{eV}$ and $\hbar^2/2m \approx 2.3 \times 10^{-3} \mu\text{m}^2\text{eV}$. The X - Y splitting parameters are $\alpha = 8 \times 10^{-3} \text{eV}$ and $a = 10^{-5}$, while the TE-TM splitting parameters are $\beta = 10^{-3} \mu\text{m}^2\text{eV}$ and $b = 7.5 \times 10^{-4} \mu\text{m}^2\text{eV}$. The Zeeman splitting $\Delta_z = 0$, unless stated otherwise. Using this set of parameters, the exceptional points are located at $k \approx 2.5 \mu\text{m}^{-1}$ and each pair is separated by $\approx 1.6 \mu\text{m}^{-1}$ in momentum space. For comparison, in the perovskite-based exciton-polariton system described in Ref. [5], the exceptional points are located at $k \approx 6.7 \mu\text{m}^{-1}$ and each pair is separated by $\approx 0.24 \mu\text{m}^{-1}$ in momentum space, making the Fermi arc difficult to see.

APPENDIX B: EXCITON-POLARITON PSEUDOSPINS

The pseudospins of the exciton polaritons can be calculated from the polarization components as

$$\begin{aligned} S_x &= \frac{|\psi^H|^2 - |\psi^V|^2}{|\psi^H|^2 + |\psi^V|^2}, \\ S_y &= \frac{|\psi^D|^2 - |\psi^A|^2}{|\psi^D|^2 + |\psi^A|^2}, \\ S_z &= \frac{|\psi^+|^2 - |\psi^-|^2}{|\psi^+|^2 + |\psi^-|^2}. \end{aligned} \quad (\text{B1})$$

Here, $|\psi^{H,V}|^2$ represents the horizontal and vertical polarization intensities, $|\psi^{D,A}|^2$ represents the diagonal and antidiagonal polarization intensities, and $|\psi^{+,-}|^2$ represents the right and left circular polarization intensities [53,54]. We note that the definitions of the in-plane Stokes vectors $[S_x, S_y]$ can be arbitrary, and the results in this work follow the convention above. Furthermore, in this manuscript, we use superscripts to denote polarization states and subscripts to denote the energy eigenstates, e.g., ψ_+ is the upper eigenstate which is not the same as the circularly polarized state ψ^+ .

APPENDIX C: TIME-EVOLUTION OPERATOR IN EXCITON-POLARITON MODEL

We consider a general two-band non-Hermitian Hamiltonian of the form

$$\mathbf{H}(\mathbf{k}) = H_0(\mathbf{k})\mathbf{I} + \vec{\mathbf{G}}(\mathbf{k}) \cdot \vec{\sigma},$$

where $\vec{\mathbf{G}}(\mathbf{k}) = [G_x(\mathbf{k}), G_y(\mathbf{k}), G_z(\mathbf{k})]$ is the effective magnetic field, $\vec{\sigma}$ is a vector of Pauli matrices, and \mathbf{I} is the 2×2 identity matrix. Dropping the \mathbf{k} dependence for brevity, the time-evolution operator can then be written as

$$e^{-i\mathbf{H}t/\hbar} = e^{-iH_0t/\hbar} \left(\mathbf{I} \cos \frac{Gt}{\hbar} - i \frac{\vec{\mathbf{G}}}{G} \cdot \vec{\sigma} \sin \frac{Gt}{\hbar} \right), \quad (\text{C1})$$

where $G = \sqrt{G_x^2 + G_y^2 + G_z^2}$.

We should also mention that this formalism does not hold at the exceptional points where the Hamiltonian can no longer be diagonalized and the two eigenstates coalesce. However, since this formalism holds in the vicinity of the exceptional points as well as for the rest of momentum space, we believe that it is an accurate approximation for the time evolution of the wave packets.

APPENDIX D: OVERLAP WITH EIGENSTATES

In a quantum system described by a non-Hermitian Hamiltonian operator, the right and left eigenstates are generally not equal and can be written as [3,4]

$$\begin{aligned} \mathbf{H}|\psi_{\pm}^R\rangle &= E_{\pm}|\psi_{\pm}^R\rangle, \\ \mathbf{H}^\dagger|\psi_{\pm}^L\rangle &= E_{\pm}^*|\psi_{\pm}^L\rangle. \end{aligned} \quad (\text{D1})$$

Instead of the usual orthonormal condition, the eigenstates obey the biorthogonal condition,

$$\langle\psi_i^L|\psi_j^R\rangle = \delta_{i,j}. \quad (\text{D2})$$

Therefore, when the system is in a superposition of the two right eigenstates $|\psi\rangle = c_+|\psi_+^R\rangle + |\psi_-^R\rangle$, the coefficients can be determined as

$$c_{\pm} = \langle\psi_{\pm}^L|\psi\rangle.$$

By taking the normalized modulus squared $|c_{\pm}|^2/(|c_+|^2 + |c_-|^2)$, we were able to calculate the ratio of each eigenstate in the wave packet. Similarly to the time-evolution operator in Appendix C, this approach fails only at the exceptional points; hence, we believe that the approximation is accurate as it holds in the vicinity of the exceptional points.

APPENDIX E: PROPOSED EXPERIMENTAL MEASUREMENT OF THE PSEUDOSPIN DEFECTS

In experiments, the probability density distribution and the pseudospin textures can be measured using a streak camera which can take a screen shot of the wave packets in both real and momentum space at a resolution of ≈ 2 ps. Since the measurements are made by taking multiple screen shots and then averaging over the time resolution, we aim to investigate whether the pseudospin defects on the imaginary Fermi arc will still appear when the fields are averaged.

Since the pseudospin of the wave packets cannot be measured in the regions with small probability density, we need to make sure that the polariton density at the location of the pseudospin defects is non-negligible. Previous work [16] shows that the larger the wave packets are, the faster they will move away from the initial COM. Therefore, we need a wave packet that is well localized in momentum space, so it will stay near the defect for a long time. However, the wave packet cannot be too focused since we still need to measure the pseudospin texture of the entire defect.

Furthermore, although it is unknown whether the change in the pseudospin textures will reach a steady state, our numerical calculations indicate that the change of the pseudospin slows down with time. Therefore, the best way to measure the pseudospin defects is to take measurements over a long time, taking care to not exceed the time after which the wave packet moves away from the imaginary Fermi arc.

To simulate an experiment, we choose a circularly polarized polariton wave packet with a width of $\sigma_k = 0.02 \mu\text{m}^{-1}$ in momentum space with initial center-of-mass momentum of $\langle\mathbf{k}\rangle = (0.215, 6.73) \mu\text{m}^{-1}$ and consider a realistic set of parameters presented in Ref. [5]. The initial condition of the wave packet is chosen so that its size is small enough so it will stay on the imaginary Fermi arc for a long time, yet not too small to be realized in experiment. The wave packet has a size of $\sigma_r = 50 \mu\text{m}$ in real space, which can be achieved in the experiments. We found that the wave packet at $t = 5$ ps is still on the imaginary Fermi arc and covers the pseudospin defect, but is starting to move away at $t = 15$ ps. Therefore, we chose to take the average of the wave packets every 2 ps from $t = 5$ to $t = 15$ ps to see if the averaged wave packet will exhibit the pseudospin defects.

The polarizations, $|\psi^{\pm}|^2$, $|\psi^{H,V}|^2$, and $|\psi^{D,A}|^2$, are therefore measured every 2 ps from $t = 5$ to $t = 15$ ps. We then take the average of these intensities, $\langle|\psi^{\pm}|^2\rangle_{\text{ave}}$, $\langle|\psi^{H,V}|^2\rangle_{\text{ave}}$, and $\langle|\psi^{D,A}|^2\rangle_{\text{ave}}$, and use them to compute the pseudospin textures. We observe that the wave packet and its time-averaged pseudospin textures take forms similar to those at $t = 5$ ps in momentum space [see Figs. 12(a)–12(d)]. Therefore, the snapshot of the wave packet at $t = 5$ ps will dominate the time-averaged measurement in momentum space. This is because the wave packets at later times have much lower intensities due to the continuing decay (negative imaginary part of eigenenergies) of the exciton polaritons. On the other hand, in the real space, the averaged wave packet and pseudospin textures do not completely agree with those at $t = 5$ ps, as seen in Figs. 12(e)–12(h). However, the pseudospin antimeron structure at the center of the wave packet still persists after the averaging. Therefore, we conclude that the pseudospin antimerons generated by non-Hermitian wave-packet dynamics can be measured experimentally in both momentum space and real space.

APPENDIX F: WAVE-PACKET TRAJECTORIES IN OTHER TWO-BAND SYSTEMS

Previous studies [16] have suggested that the wave-packet COM momenta of a non-Hermitian Dirac model follow the gradient of the imaginary part of the eigenenergies, $\nabla \text{Im } E$. Although this seems to accurately describe the trajectories of

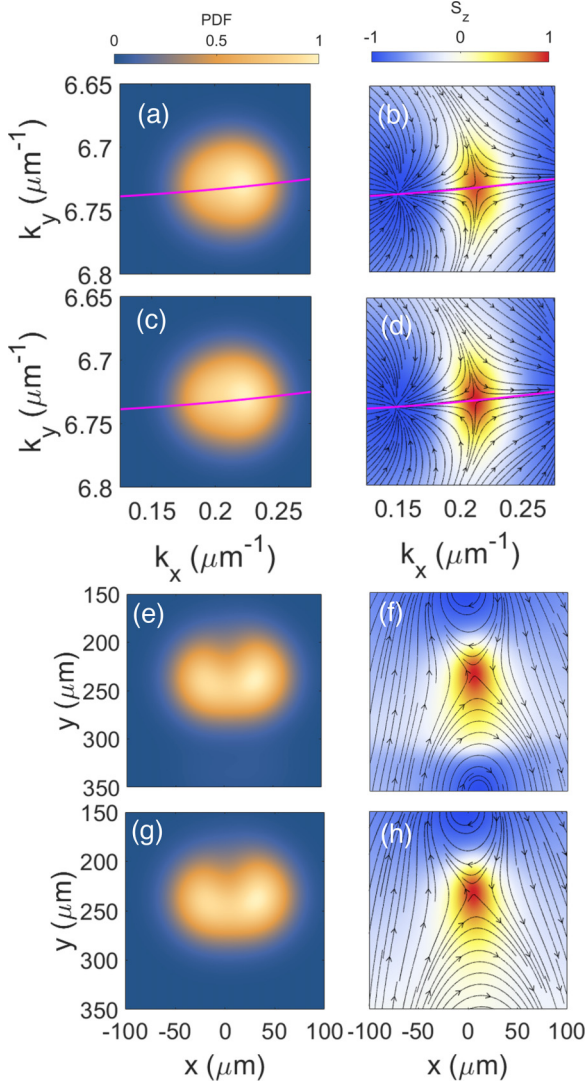


FIG. 12. The averaged wave packet and pseudospin textures of the exciton polariton in (a),(b) momentum space and (e),(f) real space. The probability density distribution and the pseudospin take similar forms to the wave packet and pseudospin textures at $t = 5$ ps in (c),(d) and (g),(h). The purple line denotes the imaginary Fermi arc.

the exciton-polariton wave packets, this is not always the case. In this section, we illustrate this point by presenting the analysis of the wave-packet dynamics in two exemplary models, i.e., a non-Hermitian Dirac model and a non-Hermitian Chern insulator. These two models have similar band structures near the origin, but their wave-packet dynamics and asymptotic behavior are qualitatively different.

1. Non-Hermitian Dirac model

We considered the Dirac model, described by the Hamiltonian

$$\mathbf{H} = \hbar c k_x \sigma_x + \hbar c k_y \sigma_y. \quad (\text{F1})$$

This model has eigenenergies of $E_{\pm} = \pm \hbar c \sqrt{k_x^2 + k_y^2}$ and has a spectral degeneracy at the origin called the Dirac point. In solid-state physics, this model describes the Dirac semimetal,

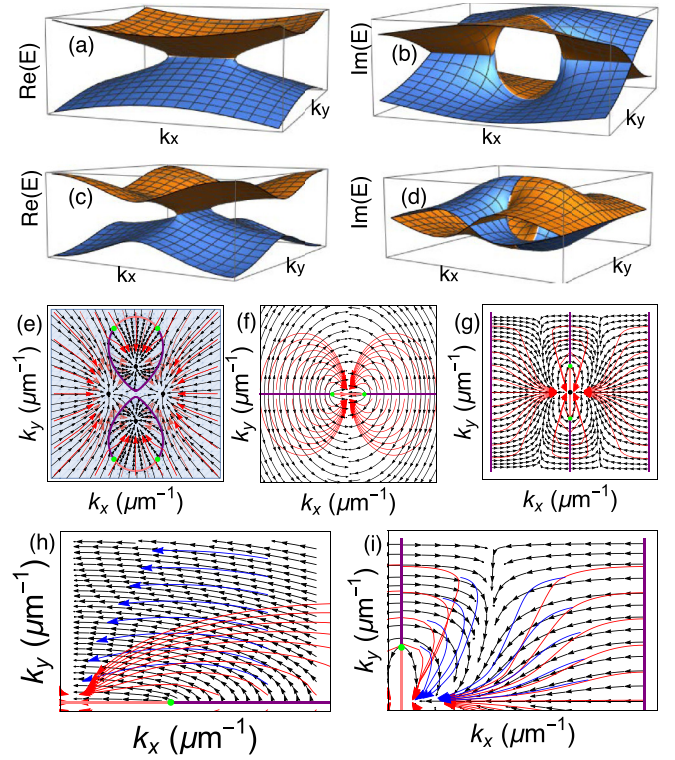


FIG. 13. (a),(b) The real and imaginary parts of the eigenenergies of the non-Hermitian Dirac model. (c),(d) The real and imaginary parts of the eigenenergies of the non-Hermitian Chern insulator in the nodal phase. (e)–(i) Wave-packet trajectories (red) with $\nabla \text{Im} E$ (black) with the Fermi arcs and exceptional points of the (e) polariton model, (f) non-Hermitian Dirac model, and (g) non-Hermitian Chern insulator. (h),(i) Wave-packet trajectories with different sets of initial COM momenta (blue arrows) in the non-Hermitian Dirac model and non-Hermitian Chern insulator, respectively, showing that they do not follow the same paths indicated by the red arrows.

which has elementary excitations of massless Dirac fermions and describes the electronic properties of graphene [55–59]. It also plays an important role in optical physics. Written in the basis of circularly polarized modes, the Dirac point describes a diabolical point which exhibits conical refraction [16,37,60,61].

We consider the non-Hermitian Dirac model described by the following Hamiltonian [16]:

$$\mathbf{H} = \hbar c k_x \sigma_x + (\hbar c k_y + i\kappa) \sigma_y + \Delta \sigma_z, \quad (\text{F2})$$

which has the eigenenergies

$$E_{\pm} = \pm \sqrt{\hbar^2 c^2 k_x^2 + (\hbar c k_y + i\kappa)^2 + \Delta^2}. \quad (\text{F3})$$

The non-Hermitian term $i\kappa \sigma_y$ splits the Dirac point at $\mathbf{k}^{DP} = (0, 0)$ into a pair of exceptional points in momentum space at $\mathbf{k}^{EP} = [\pm \sqrt{\kappa^2 - \Delta^2}/(\hbar c), 0]$.

In the non-Hermitian Dirac model, E_+ has the larger imaginary part at $k_y < 0$, while E_- has the larger imaginary part at $k_y > 0$ [see Figs. 13(a) and 13(b)]. Therefore, as time evolves, the wave packets at $k_y < 0$ tend to evolve into the upper eigenstate, while the wave packets at $k_y > 0$ tend to evolve into the lower eigenstate. Furthermore, at $\Delta = 0$, $\max(\text{Im} E)$ lies on the k_y axis. Therefore, the wave packets in the

non-Hermitian Dirac model propagate towards a line of extrema \mathbf{k}^* , unlike the wave packets in the exciton-polariton model. From Figs. 13(e) and 13(f), we can observe that unlike the trajectories of the exciton-polariton wave packets, the center-of-mass momenta of the Dirac wave packets seem to only follow $\nabla \text{Im } E_{\pm}$ initially. As time evolves, the trajectories of the wave packets start to deviate from $\nabla \text{Im } E_{\pm}$. More importantly, we can see that the trajectories of the wave packets as well as the \mathbf{k}^* points they propagate to highly depend on their initial momenta. From Fig. 13(h), we can see that the trajectories of the wave packets with a different set of initial center-of-mass momenta will not follow the same paths towards the same \mathbf{k}^* as the wave packets in Fig. 13(f).

2. Non-Hermitian Chern insulator

The non-Hermitian Chern insulator is described by the Hamiltonian [62]

$$\mathbf{H} = (m + \cos k_x + \cos k_y)\sigma_x + (i\gamma + \sin k_x)\sigma_y + \sin k_y\sigma_z \quad (\text{F4})$$

and has eigenenergies

$$E_{\pm} = \pm[(m + \cos k_x + \cos k_y)^2 + (i\gamma + \sin k_x)^2 + \sin^2 k_y]^{1/2}. \quad (\text{F5})$$

The phase diagram and edge states of this model have been extensively studied in Ref. [62]. At $m = -2$, $\gamma = 1$, there is a pair of exceptional points in the Brillouin zone at $\mathbf{k} = (0, \pm\pi/3)$ and the band structure is similar to that of the non-Hermitian Dirac model. However, unlike the Dirac model, $\text{Im } E_{\pm}$ reaches maximum at a \mathbf{k}^* in the middle of the Brillouin zone, which is also the middle of the bulk Fermi arc [see Figs. 13(c) and 13(d)].

The wave packets with different initial center-of-mass momenta in this model also follow different paths [see Fig. 13(g)]. However, unlike the non-Hermitian Dirac model, where the asymptotic behavior of the wave-packet center-of-mass momenta is sensitive to the initial conditions, the wave packets in the non-Hermitian Chern insulator seem to propagate to the same \mathbf{k}^* asymptotically.

The above analysis of the non-Hermitian Dirac model and the non-Hermitian Chern insulator shows that the center-of-mass momenta of a wave packet only follow $\nabla \text{Im } E$ of its corresponding eigenstate on a short timescale. The trajectories of the wave packets will deviate increasingly from $\nabla \text{Im } E$ with time. Furthermore, in cases where there are multiple maxima of $\text{Im } E_{\pm}$, both of the paths that the wave packets take and the \mathbf{k}^* points that the wave packets propagate towards will be sensitive to the initial conditions of the wave packets.

-
- [1] R. El-Ganainy, K. G. Makris, M. Khajavikhan, Z. H. Musslimani, S. Rotter, and D. N. Christodoulides, Non-Hermitian physics and PT symmetry, *Nat. Phys.* **14**, 11 (2018).
- [2] Ş. K. Özdemir, S. Rotter, F. Nori, and L. Yang, Parity-time symmetry and exceptional points in photonics, *Nat. Mater.* **18**, 783 (2019).
- [3] E. J. Bergholtz, J. C. Budich, and F. K. Kunst, Exceptional topology of non-Hermitian systems, *Rev. Mod. Phys.* **93**, 015005 (2021).
- [4] A. Ghatak and T. Das, New topological invariants in non-Hermitian systems, *J. Phys.: Condens. Matter* **31**, 263001 (2019).
- [5] R. Su, E. Estrecho, D. Biegańska, Y. Huang, M. Wurdack, M. Pieczarka, A. G. Truscott, T. C. H. Liew, E. A. Ostrovskaya, and Q. Xiong, Direct measurement of a non-Hermitian topological invariant in a hybrid light-matter system, *Sci. Adv.* **7**, eabj8905 (2021).
- [6] D. Leykam, K. Y. Bliokh, C. Huang, Y. D. Chong, and F. Nori, Edge Modes, Degeneracies, and Topological Numbers in Non-Hermitian Systems, *Phys. Rev. Lett.* **118**, 040401 (2017).
- [7] K. Zhang, Z. Yang, and C. Fang, Correspondence between Winding Numbers and Skin Modes in Non-Hermitian Systems, *Phys. Rev. Lett.* **125**, 126402 (2020).
- [8] F. K. Kunst, E. Edvardsson, J. C. Budich, and E. J. Bergholtz, Biorthogonal Bulk-Boundary Correspondence in Non-Hermitian Systems, *Phys. Rev. Lett.* **121**, 026808 (2018).
- [9] T. Hofmann, T. Helbig, F. Schindler, N. Salgo, M. Brzezińska, M. Greiter, T. Kiessling, D. Wolf, A. Vollhardt, A. Kabaši, C. H. Lee, A. Bilušić, R. Thomale, and T. Neupert, Reciprocal skin effect and its realization in a topoelectrical circuit, *Phys. Rev. Res.* **2**, 023265 (2020).
- [10] S. Weidemann, M. Kremer, T. Helbig, T. Hofmann, A. Stegmaier, M. Greiter, R. Thomale, and A. Szameit, Topological funneling of light, *Science* **368**, 311 (2020).
- [11] K. Zhang, Z. Yang, and C. Fang, Universal non-Hermitian skin effect in two and higher dimensions, *Nat. Commun.* **13**, 2496 (2022).
- [12] L. Jin and Z. Song, Incident Direction Independent Wave Propagation and Unidirectional Lasing, *Phys. Rev. Lett.* **121**, 073901 (2018).
- [13] B. Peng, Å. K. Özdemir, S. Rotter, H. Yilmaz, M. Liertzer, F. Monifi, C. M. Bender, F. Nori, and L. Yang, Loss-induced suppression and revival of lasing, *Science* **346**, 328 (2014).
- [14] S. Longhi, D. Gatti, and G. D. Valle, Robust light transport in non-Hermitian photonic lattices, *Sci. Rep.* **5**, 13376 (2015).
- [15] K. Kawabata, K. Shiozaki, and S. Ryu, Topological Field Theory of Non-Hermitian Systems, *Phys. Rev. Lett.* **126**, 216405 (2021).
- [16] D. D. Solnyshkov, C. Leblanc, L. Bessonart, A. Nalitov, J. Ren, Q. Liao, F. Li, and G. Malpuech, Quantum metric and wave packets at exceptional points in non-Hermitian systems, *Phys. Rev. B* **103**, 125302 (2021).
- [17] S. Longhi, Non-Hermitian skin effect and self-acceleration, *Phys. Rev. B* **105**, 245143 (2022).
- [18] J. Kasprzak, M. Richard, S. Kundermann, A. Baas, P. Jeambrun, J. M. J. Keeling, F. M. Marchetti, M. H. Szymańska, R. André, J. L. Staehli, V. Savona, P. B. Littlewood, B. Deveaud, and L. S. Dang, Bose-Einstein condensation of exciton polaritons, *Nature (London)* **443**, 409 (2006).
- [19] I. Carusotto and C. Ciuti, Quantum fluids of light, *Rev. Mod. Phys.* **85**, 299 (2013).
- [20] H. Deng, H. Haug, and Y. Yamamoto, Exciton-polariton Bose-Einstein condensation, *Rev. Mod. Phys.* **82**, 1489 (2010).

- [21] T. Gao, E. Estrecho, K. Y. Bliokh, T. C. H. Liew, M. D. Fraser, S. Brodbeck, M. Kamp, C. Schneider, S. Höfling, Y. Yamamoto, F. Nori, Y. S. Kivshar, A. G. Truscott, R. G. Dall, and E. A. Ostrovskaya, Observation of non-Hermitian degeneracies in a chaotic exciton-polariton billiard, *Nature (London)* **526**, 554 (2015).
- [22] M. S. Spencer, Y. Fu, A. P. Schlaus, D. Hwang, Y. Dai, M. D. Smith, D. R. Gamelin, and X.-Y. Zhu, Spin-orbit-coupled exciton-polariton condensates in lead halide perovskites, *Sci. Adv.* **7**, eabj7667 (2021).
- [23] L. Pickup, H. Sigurdsson, J. Ruostekoski, and P. G. Lagoudakis, Synthetic band-structure engineering in polariton crystals with non-Hermitian topological phases, *Nat. Commun.* **11**, 4431 (2020).
- [24] P. Comaron, V. Shahnazaryan, W. Brzezicki, T. Hyart, and M. Matuszewski, Non-Hermitian topological end-mode lasing in polariton systems, *Phys. Rev. Res.* **2**, 022051(R) (2020).
- [25] X. Xu, R. Bao, and T. C. H. Liew, Non-Hermitian topological exciton-polariton corner modes, *Phys. Rev. B* **106**, L201302 (2022).
- [26] S. Mandal, R. Banerjee, and T. C. H. Liew, From the topological spin-Hall effect to the non-Hermitian skin effect in an elliptical micropillar chain, *ACS Photon.* **9**, 527 (2022).
- [27] Q. Liao, C. Leblanc, J. Ren, F. Li, Y. Li, D. Solnyshkov, G. Malpuech, J. Yao, and H. Fu, Experimental Measurement of the Divergent Quantum Metric of an Exceptional Point, *Phys. Rev. Lett.* **127**, 107402 (2021).
- [28] M. Król, I. Septembre, P. Oliwa, M. Kędziora, K. Łempicka-Mirek, M. Muszyński, R. Mazur, P. Morawiak, W. Piecek, P. Kula, W. Bardyszewski, P. G. Lagoudakis, D. D. Solnyshkov, G. Malpuech, B. Piętka, and J. Szczytko, Annihilation of exceptional points from different Dirac valleys in a 2D photonic system, *Nat. Commun.* **13**, 5340 (2022).
- [29] P. Cilibrizzi, H. Sigurdsson, T. C. H. Liew, H. Ohadi, A. Askitopoulos, S. Brodbeck, C. Schneider, I. A. Shelykh, S. Höfling, J. Ruostekoski, and P. Lagoudakis, Half-skyrmion spin textures in polariton microcavities, *Phys. Rev. B* **94**, 045315 (2016).
- [30] N. Nagaosa and Y. Tokura, Topological properties and dynamics of magnetic skyrmions, *Nat. Nanotechnol.* **8**, 899 (2013).
- [31] C. Guo, M. Xiao, Y. Guo, L. Yuan, and S. Fan, Meron Spin Textures in Momentum Space, *Phys. Rev. Lett.* **124**, 106103 (2020).
- [32] Q. Zhang, Z. Xie, L. Du, P. Shi, and X. Yuan, Bloch-type photonic skyrmions in optical chiral multilayers, *Phys. Rev. Res.* **3**, 023109 (2021).
- [33] B. Göbel, I. Mertig, and O. A. Tretiakov, Beyond skyrmions: Review and perspectives of alternative magnetic quasiparticles, *Phys. Rep.* **895**, 1 (2021).
- [34] M. Król, H. Sigurdsson, K. Rechcińska, P. Oliwa, K. Tyszka, W. Bardyszewski, A. Opala, M. Matuszewski, P. Morawiak, R. Mazur, W. Piecek, P. Kula, P. G. Lagoudakis, B. Piętka, and J. Szczytko, Observation of second-order meron polarization textures in optical microcavities, *Optica* **8**, 255 (2021).
- [35] G. Panzarini, L. C. Andreani, A. Armitage, D. Baxter, M. S. Skolnick, V. N. Astratov, J. S. Roberts, A. V. Kavokin, M. R. Vladimirova, and M. A. Kaliteevski, Exciton-light coupling in single and coupled semiconductor microcavities: Polariton dispersion and polarization splitting, *Phys. Rev. B* **59**, 5082 (1999).
- [36] A. V. Kavokin, J. J. Baumberg, G. Malpuech, and F. P. Laussy, *Microcavities* (Oxford University Press, Oxford, 2017), Vol. 21.
- [37] H. Terças, H. Flayac, D. D. Solnyshkov, and G. Malpuech, Non-Abelian Gauge Fields in Photonic Cavities and Photonic Superfluids, *Phys. Rev. Lett.* **112**, 066402 (2014).
- [38] S. Klemmt, T. H. Harder, O. A. Egorov, K. Winkler, R. Ge, M. A. Bandres, M. Emmerling, L. Worschech, T. C. H. Liew, M. Segev, C. Schneider, and S. Höfling, Exciton-polariton topological insulator, *Nature (London)* **562**, 552 (2018).
- [39] H. Zhou, C. Peng, Y. Yoon, C. W. Hsu, K. A. Nelson, L. Fu, J. D. Joannopoulos, M. Soljačić, and B. Zhen, Observation of bulk Fermi arc and polarization half charge from paired exceptional points, *Science* **359**, 1009 (2018).
- [40] P. Ehrenfest, Bemerkung über die angenäherte Gültigkeit der klassischen mechanik innerhalb der Quantenmechanik, *Z. Phys.* **45**, 455 (1927).
- [41] G. Dattoli, A. Torre, and R. Mignani, Non-Hermitian evolution of two-level quantum systems, *Phys. Rev. A* **42**, 1467 (1990).
- [42] E. M. Graefe, H. J. Korsch, and A. E. Niederle, Mean-Field Dynamics of a Non-Hermitian Bose-Hubbard Dimer, *Phys. Rev. Lett.* **101**, 150408 (2008).
- [43] H. Flayac, D. D. Solnyshkov, I. A. Shelykh, and G. Malpuech, Transmutation of Skyrmions to Half-Solitons Driven by the Nonlinear Optical Spin Hall Effect, *Phys. Rev. Lett.* **110**, 016404 (2013).
- [44] S. Donati, L. Dominici, G. Dagvadorj, D. Ballarini, M. D. Giorgi, A. Bramati, G. Gigli, Y. G. Rubo, M. H. Szymańska, and D. Sanvitto, Twist of generalized skyrmions and spin vortices in a polariton superfluid, *Proc. Natl. Acad. Sci. USA* **113**, 14926 (2016).
- [45] K. Everschor-Sitte, J. Masell, R. M. Reeve, and M. Kläui, Perspective: Magnetic skyrmions—Overview of recent progress in an active research field, *J. Appl. Phys.* **124**, 240901 (2018).
- [46] A. A. Kovalev and S. Sandhoefner, Skyrmions and anti-skyrmions in quasi-two-dimensional magnets, *Front. Phys.* **6** (2018).
- [47] O. A. Tretiakov and O. Tchernyshyov, Vortices in thin ferromagnetic films and the skyrmion number, *Phys. Rev. B* **75**, 012408 (2007).
- [48] N. Mohanta, A. P. Kampf, and T. Kopp, Emergent momentum-space skyrmion texture on the surface of topological insulators, *Sci. Rep.* **7**, 45664 (2017).
- [49] R. Hertel and C. M. Schneider, Exchange Explosions: Magnetization Dynamics during Vortex-Antivortex Annihilation, *Phys. Rev. Lett.* **97**, 177202 (2006).
- [50] D. V. Vishnevsky, H. Flayac, A. V. Nalitov, D. D. Solnyshkov, N. A. Gippius, and G. Malpuech, Skyrmion Formation and Optical Spin-Hall Effect in an Expanding Coherent Cloud of Indirect Excitons, *Phys. Rev. Lett.* **110**, 246404 (2013).
- [51] E. Estrecho, M. Pieczarka, M. Wurdack, M. Steger, K. West, L. N. Pfeiffer, D. W. Snoke, A. G. Truscott, and E. A. Ostrovskaya, Low-Energy Collective Oscillations and Bogoliubov Sound in an Exciton-Polariton Condensate, *Phys. Rev. Lett.* **126**, 075301 (2021).
- [52] S. Richter, H.-G. Zirnstein, J. Zúñiga-Pérez, E. Krüger, C. Deparis, L. Trefflich, C. Sturm, B. Rosenow, M. Grundmann, and R. Schmidt-Grund, Voigt Exceptional Points in an Anisotropic ZnO-Based Planar Microcavity: Square-Root Topology, Polarization Vortices, and Circularity, *Phys. Rev. Lett.* **123**, 227401 (2019).

- [53] O. Bleu, D. D. Solnyshkov, and G. Malpuech, Measuring the quantum geometric tensor in two-dimensional photonic and exciton-polariton systems, *Phys. Rev. B* **97**, 195422 (2018).
- [54] A. Gianfrate, O. Bleu, L. Dominici, V. Ardizzone, M. De Giorgi, D. Ballarini, G. Lerario, K. W. West, L. N. Pfeiffer, D. D. Solnyshkov, D. Sanvitto, and G. Malpuech, Measurement of the quantum geometric tensor and of the anomalous Hall drift, *Nature (London)* **578**, 381 (2020).
- [55] K. S. Novoselov, A. K. Geim, S. V. Morozov, D. Jiang, Y. Zhang, S. V. Dubonos, I. V. Grigorieva, and A. A. Firsov, Electric field effect in atomically thin carbon films, *Science* **306**, 666 (2004).
- [56] K. S. Novoselov, A. K. Geim, S. V. Morozov, D. Jiang, M. I. Katsnelson, I. V. Grigorieva, S. V. Dubonos, and A. A. Firsov, Two-dimensional gas of massless Dirac fermions in graphene, *Nature (London)* **438**, 197 (2005).
- [57] Y. Zhang, Y.-W. Tan, H. L. Stormer, and P. Kim, Experimental observation of the quantum Hall effect and Berry's phase in graphene, *Nature (London)* **438**, 201 (2005).
- [58] A. H. Castro Neto, F. Guinea, N. M. R. Peres, K. S. Novoselov, and A. K. Geim, The electronic properties of graphene, *Rev. Mod. Phys.* **81**, 109 (2009).
- [59] N. P. Armitage, E. J. Mele, and A. Vishwanath, Weyl and Dirac semimetals in three-dimensional solids, *Rev. Mod. Phys.* **90**, 015001 (2018).
- [60] W. R. Hamilton, Third supplement to an essay on the theory of systems of rays, *Trans. R. Irish Acad.* **17**, 1 (1831).
- [61] H. Lloyd, On the phenomena presented by light in its passage along the axes of biaxial crystals, *Trans. R. Irish Acad.* **17**, 145 (1831).
- [62] K. Kawabata, K. Shiozaki, and M. Ueda, Anomalous helical edge states in a non-Hermitian Chern insulator, *Phys. Rev. B* **98**, 165148 (2018).